

See discussions, stats, and author profiles for this publication at: <https://www.researchgate.net/publication/44669464>

# Probing of multidrug ABC membrane transporters of single living cells using single plasmonic nanoparticle optical probes

ARTICLE *in* ANALYTICAL AND BIOANALYTICAL CHEMISTRY · AUGUST 2010

Impact Factor: 3.44 · DOI: 10.1007/s00216-010-3864-8 · Source: PubMed

CITATIONS

13

READS

18

## 6 AUTHORS, INCLUDING:



**Kerry J. Lee**

Old Dominion University

13 PUBLICATIONS 652 CITATIONS

SEE PROFILE



**Lauren Marie Browning**

Old Dominion University

11 PUBLICATIONS 603 CITATIONS

SEE PROFILE



**Feng Ding**

The University of Tennessee Health Science...

6 PUBLICATIONS 33 CITATIONS

SEE PROFILE



**Prakash D Nallathamby**

University of Notre Dame

24 PUBLICATIONS 906 CITATIONS

SEE PROFILE

# Probing of multidrug ABC membrane transporters of single living cells using single plasmonic nanoparticle optical probes

Kerry J. Lee · Lauren M. Browning · Tao Huang ·  
Feng Ding · Prakash D. Nallathamby ·  
Xiao-Hong Nancy Xu

Received: 15 March 2010 / Revised: 19 May 2010 / Accepted: 19 May 2010  
© Springer-Verlag 2010

**Abstract** Currently, molecular mechanisms of multidrug ABC (ATP-binding cassette) membrane transporters remain elusive. In this study, we synthesized and characterized purified spherically shaped silver nanoparticles (Ag NPs) ( $11.8 \pm 2.6$  nm in diameter), which were stable (non-aggregation) in PBS buffer and inside single living cells. We used the size-dependent localized surface plasmon resonance (LSPR) spectra of single Ag NPs to determine their sizes and to probe the size-dependent transport kinetics of the ABC (BmrA, BmrA-EGFP) transporters in single living cells (*Bacillus subtilis*) in real time at nanometer resolution using dark-field optical microscopy and spectroscopy (DFOMS). The results show that the smaller NPs stayed longer inside the cells than larger NPs, suggesting size-dependent efflux kinetics of the membrane transporter. Notably, accumulation and efflux kinetics of intracellular NPs for single living cells depended upon the cellular expression level of BmrA, NP concentrations, and a pump inhibitor (25  $\mu$ M, orthovanadate), suggesting that NPs are substrates of BmrA transporters and that passive diffusion driven by concentration gradients is the primary mechanism by which the NPs enter the cells. The accumulation and efflux kinetics of intracellular NPs for given cells are similar to those observed using a substrate (Hoechst dye) of BmrA, demonstrating that NPs are suitable probes for study of multidrug membrane transporters of single living cells in real-time. Unlike fluorescent probes, single Ag NPs exhibit size-dependent LSPR spectra and superior photostability, enabling

them to probe the size-dependent efflux kinetics of membrane transporters of single living cells in real-time for better understanding of multidrug resistance.

**Keywords** ABC (BmrA) transporter · Single cell imaging · Multidrug resistance · *Bacillus subtilis* · Single nanoparticle plasmonic optics · Ag nanoparticle

## Introduction

ATP-binding cassette (ABC) membrane transporters (efflux pumps) have been found in all living organisms, including bacteria and humans [1, 2]. For example, 78 ABC transporters have been reported in *B. subtilis*, and 48 ABC transporters have been identified in humans [1–4]. Some of these transporters are involved in transport of a wide variety of structurally and functionally unrelated substrates (e.g., sugars, lipids, amino-acids, proteins, or xenobiotics), including extrusion of antibiotics or chemotherapeutic agents out of cells (e.g., bacteria or tumor cells). For example, P-glycoprotein accounts for multidrug resistance (MDR) in cancer cells, leading to ineffective treatment. Dysfunction of some of these ABC transporters causes severe diseases [5–7]. Despite extensive studies, such important and fascinating multi-substrate extrusion machinery and translocation mechanisms remain not yet fully understood [1, 2, 7].

Interestingly, all ABC transporters in any living organism share a common organization, possessing four core domains: two transmembrane domains (TMD) and two nucleotide-binding domains (NBD) [8–11]. The TMDs have quite variable sequence and topology, defining the substrate binding-sites and forming the transport passageway for substrates to cross the membranes, whereas the

K. J. Lee · L. M. Browning · T. Huang · F. Ding ·  
P. D. Nallathamby · X.-H. N. Xu (✉)  
Department of Chemistry and Biochemistry,  
Old Dominion University,  
Norfolk, VA 23529, USA  
e-mail: xhxu@odu.edu  
URL: [www.odu.edu/sci/xu/xu.htm](http://www.odu.edu/sci/xu/xu.htm)

NBDs have conserved sequences, empowering the transporters by binding and hydrolyzing ATP [8, 9, 12, 13]. The similar structures and organization of ABC transporters suggest possible similar transport mechanisms.

*B. subtilis* (a Gram-positive bacterium) has a fully sequenced genome, and it is amenable to genetic manipulation [14, 15]. Therefore, *B. subtilis* has been widely used as a model organism for probing the function of prokaryotes and for better understanding of bacterial pathogenic functions (e.g., sporulation) and efflux function of multidrug membrane transporters, even though *B. subtilis* itself is not regarded as a human pathogen [16, 17].

Currently, radioactively labeled substrates ( $^{14}\text{C}$  and  $^3\text{H}$ ) and the fluorescent dyes (e.g., rhodamine 123, Fluo-3, Hoechst dyes) are common probes for investigating efflux kinetics of multidrug transporters in bacterial and mammal cells [18–22]. Fluorescent dyes, for example Hoechst dyes and ethidium bromide (EtBr), are quinolones, common substrates for multidrug membrane transporters in bacteria. The fluorescent dyes emit weak fluorescence in aqueous solution (outside cells) and become strongly fluorescent in non-polar and hydrophobic environments, especially as the dye molecules enter cells and intercalate with DNA [23]. Therefore, the time-dependent (time-course) fluorescence intensity of fluorescent dyes has been widely used to characterize efflux function of multidrug membrane transporters in bacterial and mammalian cells [18–22].

Although these conventional methods effectively provide ensemble accumulation kinetics of bulk cells, they are unable to determine transformation of pore sizes of ABC membrane transporters in response to various sizes of substrates in single living cells. Therefore, it is impossible to use them for probing size-dependent efflux kinetics of multidrug (multi-substrate) ABC membrane transporters for better understanding of their functions and molecular mechanisms. These limitations demand the development of new methods for probing the size-transformation of individual membrane transporters in single living cells in real time, in order to better understand molecular mechanisms of multidrug membrane transporters. Individual membrane transporters are likely to have unsynchronized membrane transport kinetics, underscoring the importance of probing the transport kinetics of single membrane transporters in single living cells in real time.

Currently, the sizes of membrane transporters are characterized at atomic resolution using X-ray crystallography or cryo-TEM [8, 10, 24]. However, neither method can measure real-time transport dynamics of substrates and self-assembly of pump proteins in living cells. Therefore, the mechanisms and functions of membrane transporters remain elusive, even through structures of some membrane transporters at atomic resolution are now available [8, 10, 24].

Noble metal (e.g., Ag) NPs have size-dependent optical properties, enabling us to image and determine the sizes of

single NPs at the nanometer (nm) scale in real time using dark-field optical microscopy and spectroscopy (DFOMS) [25–31]. Notably, the size-dependent localized surface plasmon resonance (LSPR) spectra (colors) of single NPs enable us to image the sizes of NPs in solution, single living cells, and embryos at nm resolution in real time [26, 28–35]. These unique features enable us to use the color (LSPR spectra) index of the multicolor NPs as a nanometer-size index to directly measure sizes of single NPs as they are transported in and out of single living cells, and thereby to determine the sizes of membrane pores at nm resolution in real-time [28, 30, 31]. Unlike fluorescent probes and semiconductor quantum dots (QDs), these noble metal NPs resist photodecomposition and blinking and have superior photostability [26, 29, 33], enabling them to serve as optical sized probes for tracking the transformation of pore sizes of membrane transporters and the size-dependent transport kinetics of efflux pumps for any desired period of time.

We have previously used the intrinsic optical properties of the noble metal NPs (e.g., Ag) for probing of sizes and transport dynamics of a single membrane transporter (MexAB-OprM) in single living cells (*P. aeruginosa*, Gram-negative bacterium), and the transformation of pore sizes of their cellular membranes induced by antibiotics (e.g., aztreonam, chloramphenicol) at sub-100 nm spatial resolution and millisecond temporal resolution [28, 30, 31].

In this study, we synthesized and characterized stable and purified spherical Ag NPs with an average diameter of  $11.8 \pm 2.6$  nm (8.4–31.5 nm). We used their size-dependent LSPR spectra to determine the sizes of single NPs at nm resolution in real time, when they were in and out of single living cells, which enabled us to probe the size-dependent efflux kinetics of BmrA (one of the ABC membrane transporters) of single living bacterial cells (*B. subtilis*, Gram-positive bacterium). We also used the Ag NP probes to characterize BmrA fused with EGFP via its C or N-terminus (Ct-BmrA-EGFP, or Nt-BmrA-EGFP) and to compare them with BmrA, aiming to determine whether the fused BmrA-EGFP maintains the efflux function of BmrA. We need to first determine whether BmrA-EGFP maintains the original efflux functions of BmrA, before we can use fused EGFP to visualize the BmrA locations and to characterize BmrA topologies, as those reported for other ABC transporters [36–39].

## Experimental section

### Reagents and cell lines

Live/dead *bacLight* viability and counting assay and Hoechst 33342 were purchased from Invitrogen; all other reagents were purchased from Sigma–Aldrich, and used as

received. For cell lines of *Bacillus subtilis*, WT (BmrA) were purchased from Bacillus Genome Stock Center (BGSC), and  $\Delta$ BmrA (previously named  $\Delta$ YvcC, a mutant strain that is void of the BmrA) were provided by J.M. Jault [40]. The cell lines of Ct-BmrA-EGFP (54A, a mutant with over expression of BmrA with its C-terminal fusion with EGFP) and Nt-BmrA-EGFP (29A, a mutant with over expression of BmrA with its N-terminal fusion with EGFP) were constructed in our laboratory. The design and characterization of Nt-BmrA-EGFP and Ct-BmrA-EGFP will be fully described and reported elsewhere.

### Synthesis and characterization of Ag NP optical probes

Silver NPs were synthesized and washed as described previously [29, 33]. The purified Ag NPs were dispersed in the PBS buffer (0.5 mM phosphate buffer, 1.5 mM NaCl, pH=7.0). We characterized the sizes, concentrations and number of single NPs in the buffer over time to determine the stability (non-aggregation) of NPs in the buffer. The sizes of single NPs were determined using high-resolution transmission electron microscopy (HRTEM) (FEI Tecnai G2 F30 FEG) and dynamic light scattering (DLS) (Nicomp 380ZLS particle sizing system). The concentrations of NPs were measured and calculated, as described previously [33, 41]. Plasmonic absorption and scattering properties of bulk NPs were characterized using UV–visible spectrometry (Hitachi).

The plasmonic images and LSPR spectra of single NPs were acquired using DFOMS equipped with CCD camera (Micromax, Roper Scientific) and multiple-spectra imaging system (Nuance, CRI) [26, 35]. The design and construction of DFOMS have been fully described in our previous studies [22, 25, 26, 28–33, 42]. The dark-field optical microscope was equipped with a dark-field condenser (oil 1.43–1.20, Nikon) and a 100 $\times$  objective (Nikon Plan fluor 100 $\times$  oil, iris, SL. N.A. 0.5–1.3, W.D. 0.20 mm) with a depth of field (focus) of 190 nm.

### Cell culture and preparation

We pre-cultured the cells in an Erlenmeyer flask (250 mL) containing 20 mL L-broth (LB) medium (1% tryptone peptone, 0.5% yeast extract, 0.5% NaCl, pH=7.2) in a shaker (Lab-line Orbit Envivon-Shaker; 150 rpm, 37°C) for 12 h. We then cultured the cells (WT and  $\Delta$ BmrA) in the LB medium for another 8 h, and cultured the Ct-BmrA-EGFP and Nt-BmrA-EGFP cells in the medium containing 1% xylose for another 8 h to ensure the full expression of the EGFP. We harvested the cultured cells using centrifugation (Beckman Model J2-21 Centrifuge, JA-14 rotor, at 7500 rpm, 23°C, 10 min), washed the cells with the PBS buffer three times, and finally re-suspended the cells in the

buffer. The final concentration of the cells was adjusted to  $OD_{600\text{ nm}} = 0.1$ , and used for the entire study.

### Imaging of single NPs in single living cells and probing cellular viability

Cell suspensions ( $OD_{600\text{ nm}} = 0.1$ ) containing 0.7 and 1.4 nM Ag NPs in the absence and presence of orthovanadate (25  $\mu$ M) were prepared. The timer was started to record the incubation time as the NPs were added to the cell suspension.

We transferred the mixture (20  $\mu$ L) into a freshly prepared microchamber and continuously imaged and acquired LSPR spectra of single NPs in and out of single living cells in real time for 3 h using DFOMS, which enabled us to determine the sizes and positions of single NPs simultaneously. The construction of the microchamber for imaging of single bacterial cells over time was fully described in our previous studies [22, 28, 30, 31, 42, 43]. We could achieve temporal resolution up to 5 ms with sufficiently high signal-to-noise ratios for continuous imaging of the transport of single NPs in and out of single living cells. However, we found that the transport of single NPs in and out of single living cells (*B. subtilis*) was not a rapid process and a temporal resolution of seconds to two minutes was sufficient to track their transport in real time. This approach enabled us to avoid generating single data files of huge sizes (> 200 GB) that would be unnecessary and hard to handle and analyze.

We also sampled the mixture (20  $\mu$ L) into a freshly prepared microchamber every 20 min and imaged the cells on ten representative locations in the microchamber using DFOMS equipped with a CCD camera. This approach enabled us to image massive numbers of cells (3000 cells) for each sample to gain sufficient statistics for probing the accumulation rates of bulk cells at single-cell resolution. We determined intracellular NPs and plotted them versus time to measure the accumulation rates of single NPs for the cells over time (accumulation rate = slope of the plot).

At the end of each experiment, the viability of the cells was characterized using live/dead *BacLight* bacterial viability and counting assay [44]. We imaged the cells using dark-field optical microscopy and epi-fluorescence microscopy, and counted the green fluorescent cells (peak wavelength of fluorescence spectra of SYTO9,  $\lambda_{\text{max}} = 520$  nm) and red fluorescent cells (peak wavelength of fluorescence spectra of propidium iodide,  $\lambda_{\text{max}} = 610$  nm) as live and dead cells, respectively.

### Fluorescence spectroscopy measurements

Time-dependent (time-course) fluorescence intensity of Hoechst 33342 (2  $\mu$ M) incubated with the cells ( $OD_{600\text{ nm}} = 0.1$ ) was measured at a 3-s data acquisition interval in

real-time using a fluorescence spectrometer (Perkin–Elmer LS50B). The excitation and emission wavelengths were 350 and 455 nm, respectively.

### Data analysis and statistics

For characterization of sizes, shapes, and LSPR spectra of single NPs using HRTEM and DFOMS, a minimum of 100 Ag NPs were imaged for each measurement. Each measurement was repeated three times. Thus, 300 NPs were characterized for each solution.

We acquired ~30 cells in a single CCD image in real time simultaneously. Therefore, we studied the transport of single NPs in and out of ~30 of single living cells for each measurement. We repeated the experiment three times and hence ~90 cells were studied to determine the transport of single NPs in and out of single living cells in real time.

We also acquired ten representative images of each cell suspension incubated with 0.7 or 1.4 nM Ag NPs every 20 min for 3 h to study accumulation rates of intracellular NPs in single living cells in the presence or absence of the inhibitor (orthovanadate, 25  $\mu$ M). Therefore, a minimum of ~300 cells was imaged every 20 min, and 2700 cells were studied over 3 h for each measurement. Each experiment was repeated three times. Thus, 8100 cells were studied for each sample, which enabled us to gain sufficient statistics for probing accumulation rates and efflux kinetics of bulk cells at single-cell resolution. We analyzed the number of intracellular NPs in 900 cells (300 cells for each measurement) during each 20 min, plotted them over time, and used the slope of the plots to determine the accumulation rates of intracellular NPs for the cells in the presence and absence of the pump inhibitor (orthovanadate, 25  $\mu$ M). The equilibrium times of accumulation of NPs in the cells were determined at the times when the accumulation rates of intracellular NPs remained unchanged over time. The amount of accumulated intracellular NPs for each strain refers to the amount of intracellular NPs at the equilibrium time.

For the study of the viability of single cells, a minimum of 300 cells incubated with 1.4 nM Ag NPs for 12 h was assayed for each measurement. Each measurement was repeated three times. Thus, 900 cells were assayed for each sample.

## Results and discussion

### Synthesis and characterization of single Ag NP optical probes

We synthesized spherical Ag NPs and purified them by washing the NPs with nanopure deionized (DI) water using centrifugation. This approach enables us to remove any

residual chemicals from the synthesis and to produce highly purified NPs. We found that the purified Ag NPs were stable in DI water for months, as we reported previously [29]. In order to maintain the viability of bacterial cells (*B. subtilis*), the cells must be suspended and incubated in cell culture media or PBS buffer (0.5 mM phosphate buffered saline, 1.5 mM NaCl). Notably, the studies of accumulation and efflux kinetics of multidrug membrane transporters (efflux pumps) in bacterial cells (Gram-negative or Gram positive bacteria) using fluorescence molecules have been carried out in buffer solution (PBS buffer), but not in cell culture medium [19, 40, 42, 43, 45, 46].

Given concentrations and stages of the cells (e.g.,  $OD_{600\text{ nm}} = 0.1$ ) must be incubated with given concentrations of fluorescent molecules (substrates), in order to determine the dependence of accumulation and efflux kinetics of membrane transporters on substrate concentrations and on the expression level of membrane transporters in given cells. Note that the cells grow and divide in the medium, leading to the change of cell concentrations, which makes it nearly impossible to compare results among experiments. Therefore, the cells are typically harvested from cell culture media, well rinsed, and dispersed in the PBS buffer with given concentrations (e.g.,  $OD_{600\text{ nm}} = 0.1$ ) for probing of transport kinetics of membrane transporters in living cells [19, 40, 42, 43, 45, 46].

It is crucial to ensure that single Ag NPs are stable (non-aggregated) in the PBS buffer over time, in order to utilize the size-dependent LSPR spectra (colors) of single NPs to determine their sizes, to probe the pore sizes of membrane transporters, and to study size-dependent and concentration-dependent efflux kinetics of single membrane transporters of single living cells in the buffer.

We characterized the sizes, shapes, and LSPR spectra of purified Ag NPs in the buffer for 24 h at single-NP resolution using HRTEM and DFOMS. This approach enabled us to study the stability (non-aggregation) of purified Ag NPs in the buffer for 24 h at single-NP resolution. The results in Figs. 1A and B show single spherical NPs with an average diameter of  $12.1 \pm 4.8$  nm, ranging from 8.4 to 31.5 nm. The representative optical images of single NPs in Fig. 1C show that the majority of NPs are plasmonic blue NPs with some being green and few red NPs. Histograms of color (size) distribution of single NPs (Fig. 1D) from 20 images similar to that in Fig. 1C, show 74% blue, 22% green, and 4% red NPs, and 71% blue, 24% green, and 5% red NPs, before and after the NPs were dispersed in the buffer for 24 h, respectively.

We correlated the size distribution of single NPs measured by HRTEM (Fig. 1B) with the color (peak-wavelength of LSPR spectra) distribution of single NPs characterized using DFOMS (Fig. 1D), and found that blue, green, and red NPs were correlated with NPs with diameters of 5–14 nm, 14–20 nm, and 20–32 nm, respectively [30, 35]. Therefore, we



used the LSPR spectra (colors) of single NPs to determine their sizes in real-time, and used them as sized-probes to characterize the transformation of pore sizes of membrane transporters in single living cells and to study the size-dependent transport kinetics of multidrug membrane transporters (BmrA) of single living cells.

We also characterized the sizes, optical properties and stability (non-aggregation) of bulk Ag NPs in the buffer for 24 h using UV–visible absorption spectroscopy and DLS. The UV–visible absorption spectra of purified Ag NPs before and after their incubation in the buffer for 24 h show unchanged peak absorbance of 1.047 and 1.043 at 392 nm (Fig. 1E), respectively. The size distributions of the Ag NPs before and after their incubation in the buffer for 24 h characterized using DLS show the same distribution range, with the average diameters of NPs at  $11.8 \pm 2.6$  nm and  $11.8 \pm 2.8$  nm (Fig. 1F), respectively. The results indicate that the sizes of Ag NPs in the buffer remain unchanged for 24 h. Interestingly, unlike our previous observations [29], the diameters of NPs measured in solution by DLS were slightly smaller than those measured under vacuum using HRTEM,

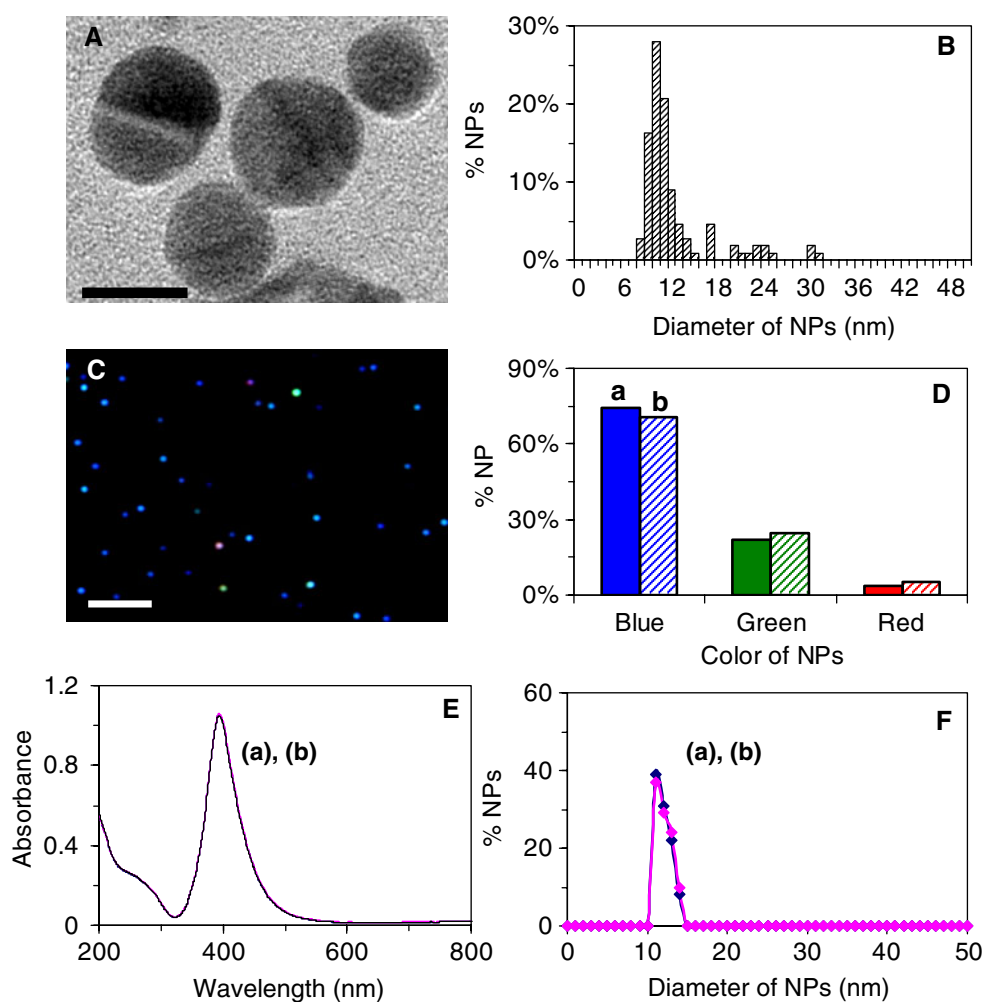
which may be attributed to the negligible portion of larger NPs (20–32 nm in diameter) for ensemble measurements of DLS. In this study, the NPs in the buffer solution were used to characterize the efflux function of the BmrA transporter in single living bacterial cells (*B. subtilis*). Therefore, the average diameter of NPs is the one ( $11.8 \pm 2.6$  nm) measured in solution using DLS. Taken together, the results in Fig. 1 show that purified Ag NPs are stable in the buffer solution for 24 h.

#### Real-time probing of size-dependent efflux kinetics of BmrA using single Ag NPs

We used the size-dependent LSPR spectra (plasmonic properties) of single Ag NPs to probe the size-dependent efflux function of BmrA by incubating the Ag NPs with the living cells ( $OD_{600\text{ nm}} = 0.1$ ) and tracking single NPs in and out of single living cells in real time.

The representative optical images of the cells with single intracellular and extracellular NPs in Figs. 2A and B show cross-sections of single rod-like bacterial cells. The size of

**Fig. 1** Characterization of sizes, shapes and plasmonic optical properties of single Ag NPs, and their stability (non-aggregation) in PBS buffer. NPs dispersed in the PBS buffer for (a) 0 min and (b) 24 h. (A) Representative HRTEM image and (B) histogram of the size distribution of Ag NPs show nearly uniform spherically shaped NPs with an average diameter of  $12.38 \pm 4.3$  nm. (C) Representative dark-field optical image of single NPs and (D) histograms of color distribution of single NPs show: (a) 74% blue, 22% green, and 4% of red NPs; and (b) 71% blue, 24% green, and 5% of red NPs. (E) UV–visible absorption spectra of 1.4 nM Ag NPs show peak absorbance of (a) 1.047 at 392 nm and (b) 1.043 at 392 nm. (F) Histograms of size distribution of single NPs in solution measured using DLS show the average diameters of NPs at (a)  $11.8 \pm 2.6$  nm and (b)  $11.8 \pm 2.8$  nm. The scale bars are 10 nm in (A) and 10  $\mu$ m in (C). The scale bar in (C) shows the distances among single NPs, but not the sizes of NPs, because they are imaged under the optical diffraction limit



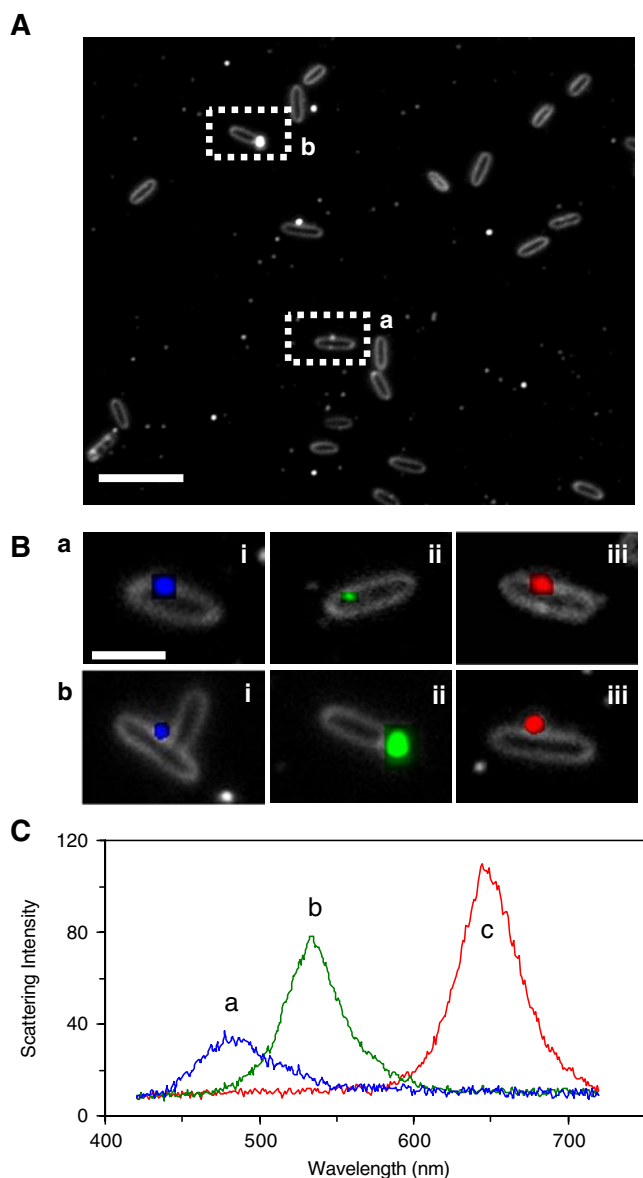


**Fig. 2** Imaging of single intracellular and extracellular Ag NPs for single living bacterial cells using DFOMS. **(A)** The representative optical image of the cells (BmrA,  $OD_{600\text{ nm}} = 0.1$ ) incubated with 1.4 nM Ag NPs shows: (a) intracellular and (b) extracellular NPs, in dotted rectangles. **(B)** Zoom-in images of single cells illustrate (a) intracellular and (b) extracellular NPs. **(C)** LSPR spectra of single Ag NPs show peak wavelengths of representative blue, green, and red NPs at 481, 535, and 649 nm, respectively. The scale bars in **(A)** and **(B)** are 10 and 2  $\mu\text{m}$ , respectively

single bacterial cells is about 2  $\mu\text{m}$  in length and 0.5  $\mu\text{m}$  in width with the thickness of their cellular membranes is about 9 nm. Notably, the top and bottom membranes of single living cells are invisible under dark-field illumination, which demonstrates that the focal plane (depth of field at 190 nm) of dark-field microscopy indeed enables us to image the thin-layer sections of single living bacterial cells and to visualize single NPs on the thin-layer section of single cells.

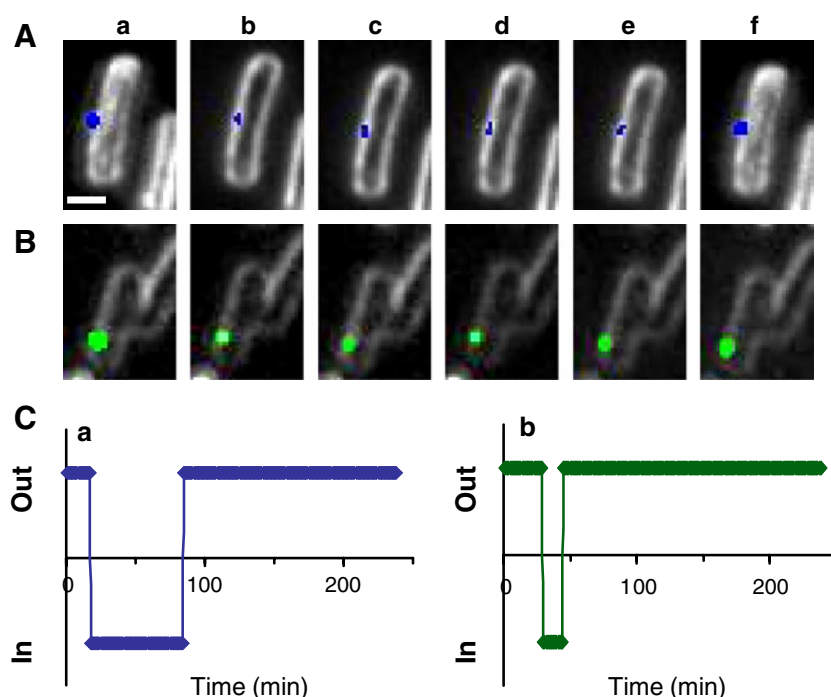
The dark-field microscope illumination needs to pass through the cellular membrane in order to irradiate intracellular NPs, and light scattering of intracellular NPs requires passage through the membrane in order to be imaged by the detector. The cellular membrane absorbs photons, leading to lower scattering intensity of intracellular NPs (dimmer). In contrast, the scattering intensity of the extracellular NPs on the membrane contains the scattering intensity of NPs and cellular membrane, leading to radiating imaging and higher scattering intensity. These features allow us to distinguish between the intracellular and extracellular NPs. The intracellular NPs are dimmer and more blurry than NPs in solution, as shown in Fig. 2A-a and B-a. In contrast, the extracellular NPs are radiating and much brighter than NPs in solution, as shown in Figs. 2A-b and B-b. Notably, we have validated these imaging approaches for determining intracellular and extracellular NPs by imaging ultra-thin sections of cells using TEM [30].

The representative LSPR spectra of single NPs in Fig. 2C show the peak wavelengths ( $\lambda_{\text{max}}$ ) at 481 (blue), 535 (green), and 649 nm (red NPs). Using the LSPR spectra (colors) of single Ag NPs, we identified the Ag NPs over any other possible cellular debris and vesicles, which do not have plasmonic properties and thus appear white under dark-field illumination. Furthermore, size-dependent plasmonic spectra enable us to determine the sizes of single NPs in real-time using DFOMS via the calibration curves of the peak wavelength ( $\lambda_{\text{max}}$ ) of LSPR spectra of single NPs versus their sizes, as we reported previously [28–31, 35]. The sizes of single blue, green, and red NPs in Fig. 2C are 13.3, 21.8, and 31.5 nm, respectively.

We incubated WT BmrA cells ( $OD_{600\text{ nm}} = 0.1$ ) with 1.4 nM Ag NPs and continuously imaged single NPs in and out of single living cells in real time. Snap shots from real-time videos in Figs. 3A and B show representative single blue and green NPs in and out of single living cells, respectively. The plots of single NPs in and out of single living cells over time (Fig. 3C) show that the blue NP stays inside the cell for 66 min, whereas the green NP stays inside the cell for 14 min. The LSPR spectra of the blue and green NPs, similar to that in Fig. 2C, show the peak wavelength ( $\lambda_{\text{max}}$ ) at 479 nm and 540 nm, respectively. We determined the sizes of single blue and green NPs as 13.0 and 22.6 nm, respectively, using the correlation of sizes of single NPs determined by HRTEM with the peak wavelength of LSPR spectra (colors) of single NPs measured using DFOMS, as we reported previously [30, 35]. The results show that the smaller NPs stay inside the cell longer than larger NPs, suggesting size-dependent efflux kinetics of BmrA and indicating that smaller NPs are more biocompatible with the cells and may be more suitable carriers for drug delivery.

Taken together, plasmonic Ag NPs offer the feasibility of probing of size-dependent efflux kinetics of membrane

**Fig. 3** Real-time probing of BmrA membrane transporter of single living cells using single Ag NPs by DFOMS. Snapshots of sequential images of (A) a single blue NP (13.0 nm in diameter) in and out of single living BmrA cells at (a) 18.0, (b) 32.0, (c) 47.0, (d) 60.0, (e) 74.0, and (f) 83.0 min; and (B) a single green NP (22.6 nm in diameter) in and out of single live cells at (a) 30.0, (b) 33.0, (c) 35.0, (d) 38.0, (e) 41.0, and (f) 44.0 min. (C) Plots of imaging of in and out of single NPs in (A and B) versus time show the duration of single blue and green NPs staying inside the cells: (a) 66.0 and (b) 14.0 min, respectively



transporters in single living cells in real time. Unlike fluorescence probes (e.g., Hoechst dyes), single Ag NPs have size-dependent LSPR spectra and they are photostable (non-photodecomposition and non-blinking) [26, 29, 33]. These superior properties enable us to determine the sizes of single NPs in and out of single living cells in real-time, and use them to mimic various sizes of antibiotics (drugs) for probing efflux functions of multidrug membrane transporters

Probing of dependence of accumulation rates of NPs on expression level of BmrA

To determine whether BmrA and BmrA-EGFP are responsible for extrusion of NPs out of living cells, we studied the dependence of the accumulation kinetics of intracellular NPs upon the expression level of BmrA and BmrA-EGFP in bulk living cells at single living cell resolution. The results in Fig. 4A show that  $\Delta$ BmrA (strain of deleted BmrA) cells accumulate the highest amount of the intracellular NPs over time and have the highest accumulation rate (slope of the plot) of intracellular NPs, whereas the Nt-BmrA-EGFP cells (over expression level of BmrA with its N-terminal fusion with EGFP) accumulate the lowest amount of intracellular NPs and have the lowest accumulation rate.

Interestingly, the accumulation rate and amount of intracellular NPs in Nt-BmrA-EGFP cells are slightly lower than the WT (normal expression level of BmrA), whereas the accumulation rate in WT cells is slightly lower than Ct-BmrA-EGFP cells (over expression level of BmrA with its C-terminal fusion with EGFP). The results suggest that WT (BmrA), Nt-BmrA-EGFP, and Ct-BmrA-EGFP cells extrude the intracel-

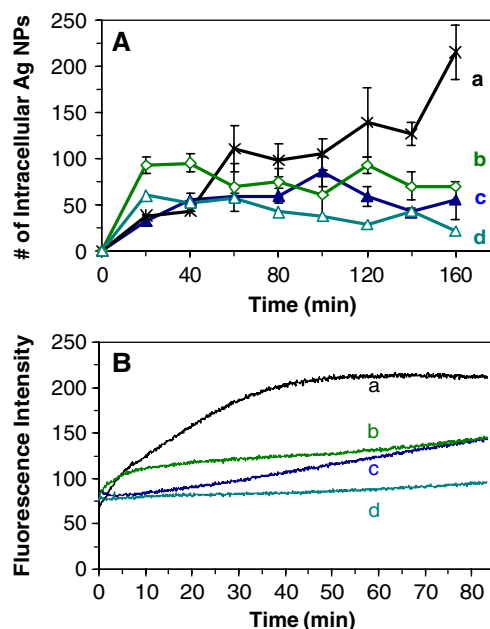


**Fig. 4** Study of the dependence of accumulation and efflux kinetics of single Ag NPs and fluorescent dye (Hoechst 33342) molecules on the expression level of BmrA. (A) Plots of number of intracellular Ag NPs versus time and (B) plot of fluorescence intensity versus time for: (a)  $\Delta$ BmrA, (b) Ct-BmrA-EGFP, (c) WT-BmrA, and (d) Nt-BmrA-EGFP cells, show that accumulation kinetics of intracellular NPs and fluorescence dye molecules in single living cells depend on cellular expression level of BmrA. In (A), the points with error bars represent the averages of experimental measurements with their standard deviations; the lines are added to guide the trend. At each point (every 20 min), 900 cells were analyzed



lular NPs, leading to less accumulation of intracellular NPs than  $\Delta$ BmrA cells. The results indicate that Nt-BmrA-EGFP and Ct-BmrA-EGFP maintain the efflux function of BmrA, and the N-terminal fusion generates less steric effects on the efflux function of BmrA than C-terminal fusion.

The sizes of NPs are about ten times larger than those of conventional antibiotics. To determine whether the NPs are suitable substrates to mimic various sizes of antibiotics for probing the efflux functions of BmrA, we used a fluorescent probe (Hoechst 33342) to study the dependence of accumulation kinetics on the cellular expression level of BmrA for probing the efflux function of BmrA and BmrA-EGFP membrane transporters. The Hoechst dye is a well-known substrate of BmrA (ABC) membrane transporter and has been widely used for probing the accumulation and efflux function of BmrA [20, 40]. The Hoechst dye emits weak fluorescence in aqueous solution (outside the cells), and its fluorescence intensity increases substantially (up to 10-fold) as the dye molecules enter the cells and intercalate with DNA [23]. Therefore, one can use the fluorescence intensity of the Hoechst dye to monitor intracellular accumulation of dye molecules [20, 40]. By probing the dependence of the accumulated amount of the intracellular dye molecules on the expression level of BmrA membrane transporters, we determined the efflux kinetics of BmrA and BmrA-EGFP.

The results in Fig. 4B show that  $\Delta$ BmrA cells accumulate the largest amount of intracellular dye molecules with the highest rate of accumulation (slope

of the curve), whereas Nt-BmrA-EGFP cells accumulate the lowest amount of intracellular dye molecules with the lowest rate of accumulation. Notably, Nt-BmrA-EGFP cells have slightly lower accumulation rate and lower amount of the intracellular dye molecules than WT cells, which have slightly lower ones than Ct-BmrA-EGFP cells. The results suggest that WT (BmrA), Nt-BmrA-EGFP, and Ct-BmrA-EGFP extrude the dye molecules and thereby they accumulate fewer intracellular dye molecules than  $\Delta$ BmrA cells, demonstrating that N-terminal or C-terminal BmrA fusion with EGFP maintains the efflux function of BmrA, and N-terminal fusion has less effect on the efflux function of BmrA than C-terminal fusion. Therefore, Nt-BmrA-EGFP and Ct-BmrA-EGFP cells become two new strains of BmrA available for further characterization of locations, structures, and functions of BmrA. The results in Fig. 4B are similar to those observed using single NP optical probes (Fig. 4A), suggesting that single NP optical probes are well suited substrates for probing the efflux function of multidrug membrane transporters.

Unlike fluorescence probes, Ag NPs offer size information about the membrane permeability and substrates of the membrane transporters. The NPs, with sizes ranging from 8.4 to 31.5 nm, can enter the cells and be extruded out of the cells by BmrA and BmrA-EGFP transporters. Notably, endocytosis, pinocytosis, and exocytosis, which are widely reported in eukaryotes, do not exist in prokaryotes (bacterial

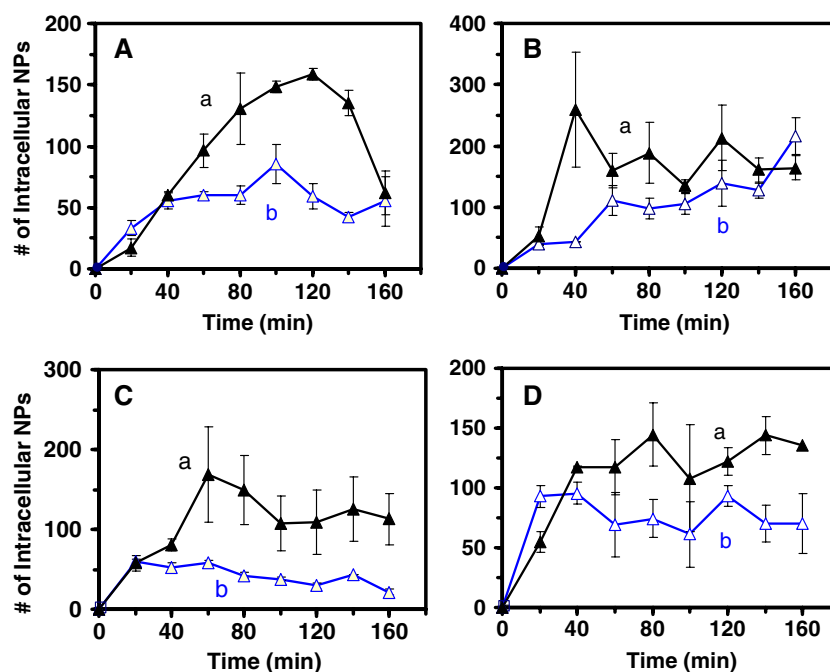
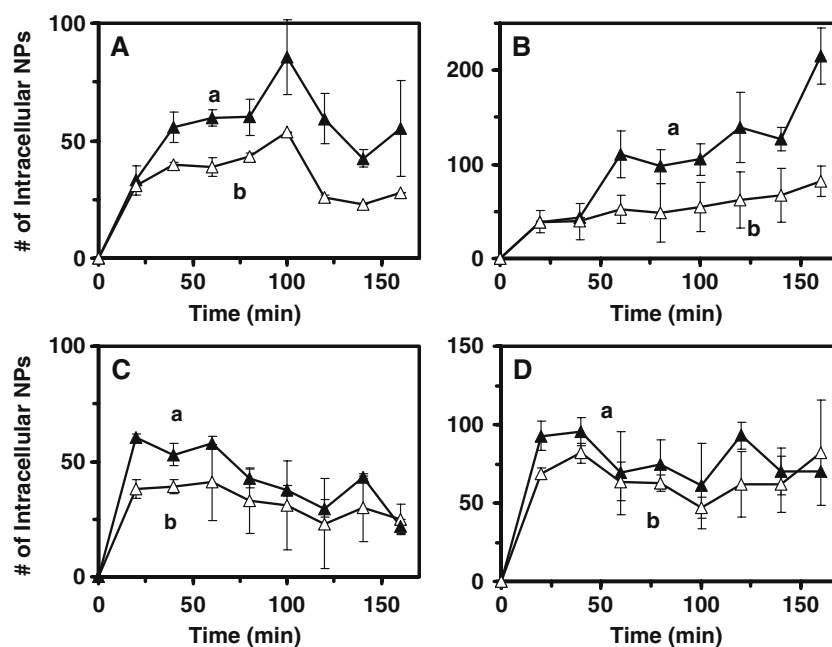


**Fig. 5** Probing of inhibitory effects of an inhibitor on accumulation and efflux kinetics of single Ag NPs for single living cells. Plots of intracellular Ag NPs versus time: (A) BmrA, (B)  $\Delta$ BmrA, (C) Ct-BmrA-EGFP, and (D) Nt-BmrA-EGFP, (a) in the absence (empty triangles) and (b)

presence (filled triangles) of the inhibitor (25  $\mu$ M, orthovanadate). The points with error bars represent the averages of experimental measurements with their standard deviations; the lines are added to guide the trend. At each point (every 20 min), 900 cells were analyzed

**Fig. 6** Study of concentration-dependent accumulation and efflux kinetics of single Ag NPs for single living cells. Plots of intracellular Ag NPs versus time: (A) BmrA, (B)  $\Delta$ BmrA, (C) Ct-BmrA-EGFP, and (D) Nt-BmrA-EGFP cells, incubated with (a) 1.4 (filled triangles) and (b) 0.7 nM (empty triangles) Ag NPs. The points with error bars represent the averages of experimental measurements with their standard deviations; the lines are added to guide the trend. At each point (every 20 min), 900 cells were analyzed



cells). Therefore, these processes are not responsible for the transport of NPs in and out of the bacterial cells (*B. subtilis*).

#### Study of effect of pump inhibitor on accumulation rates of NPs in single living cells

To determine whether BmrA and BmrA-EGFP membrane transporters are specifically responsible for the efflux of NPs, we studied the accumulation kinetics of the NPs in BmrA (WT),  $\Delta$ BmrA, Nt-BmrA-EGFP, and Ct-BmrA-EGFP living cells in the presence of a pump (ATPase) inhibitor, orthovanadate [47, 48]. The results in Fig. 5A show the higher accumulation rate of the NPs in the cells (WT-BmrA) in the presence of orthovanadate (Fig. 5A-a) than in its absence (Fig. 5A-b). In contrast, no significant change of accumulation of NPs in  $\Delta$ BmrA cells was observed in the presence of the inhibitor (Fig. 5B).

Similar to WT cells, higher accumulation of NPs in Ct-BmrA-EGFP and Nt-BmrA-EGFP cells was observed in the

presence of the inhibitor than its absence (Figs. 5C and D, respectively). These results show that the inhibitor affects the efflux of NPs by Ct-BmrA-EGFP, Nt-BmrA-EGFP, and WT-BmrA transporters, suggesting that BmrA and BmrA-EGFP membrane transporters are indeed responsible for the efflux of NPs out of the cells. These results demonstrate that the NPs are the substrates of BmrA, and they are suitable optical probes to study efflux function of BmrA membrane transporters in single living cells.

#### Study of concentration-dependent accumulation rates of NPs in single living cells

We also investigated the dependence of accumulation rates of NPs on their concentrations (doses), in order to determine molecular mechanisms of entry of NPs into single living cells, and to compare them with those observed for antibiotics. We used two concentrations of NPs (0.7 and 1.4 nM) and studied their

**Table 1** Summary of accumulation rates and equilibrium times of single NPs in single living cells

$C_{\text{Ag NPs}}$ (nM)	Inhibitor <sup>a</sup> ( $\mu$ M)	Accumulation rate (NPs min <sup>-1</sup> )				Equilibrium time (min)			
		WT	$\Delta$ BmrA	Ct <sup>b</sup>	Nt <sup>c</sup>	WT	$\Delta$ BmrA	Ct <sup>b</sup>	Nt <sup>c</sup>
0.7	0	1.1	1.6	1.0	1.1	40	60	40	40
1.4	0	1.5	1.8	1.3	1.2	40	60	40	40
1.4	25	1.7	1.8	1.9	2.1	80	120	80	80

<sup>a</sup> Orthovanadate

<sup>b</sup> Ct-BmrA-EGFP: cells with the over-expression of C-terminus BmrA fused with EGFP

<sup>c</sup> Nt-BmrA-EGFP: cells with the over-expression of N-terminus BmrA fused with EGFP

accumulation rates in BmrA (WT),  $\Delta$ BmrA, Ct-BmrA-EGFP, and Nt-BmrA-EGFP cells. The results in Fig. 6 show the dependence of the number of intracellular NPs on NP concentrations for all strains of cells, and the number of intracellular NPs increases as the concentration of NPs increases, suggesting that passive diffusion may play a role in the transport of extracellular NPs into the cells, similar to passive diffusion of antibiotics into the cells.

The lowest number of intracellular NPs and lowest accumulation rates are observed in Nt-BmrA-EGFP (Fig. 6D), whereas the highest number of intracellular NPs and highest accumulation rates are found in  $\Delta$ BmrA (Fig. 6B). Notably, the number of intracellular NPs at the equilibrium time, and accumulation rates in BmrA (WT) and Ct-BmrA-EGFP cells are similar to those observed in Nt-BmrA-EGFP. The results suggest that  $\Delta$ BmrA cells are unable to extrude the NPs out of the cells, because of the absence of the BmrA transporter, which leads to the highest accumulation of intracellular NPs. In contrast, the over-expression of Nt-BmrA-EGFP transporter effectively extrudes the NPs out of the cells, leading to the lowest accumulation of intracellular NPs. BmrA (WT) and Ct-BmrA-EGFP transporters extrude NPs out of the cells (Figs. 6A and C), leading to the lower accumulation of intracellular NPs than  $\Delta$ BmrA cells. Therefore, the accumulation rates of intracellular NPs in BmrA (WT) and Ct-BmrA-EGFP cells are similar to those observed in Nt-BmrA-EGFP. As observed in Figs. 4A and 5, the results in Fig. 6 also show the dependence of accumulation rates of intracellular NPs on the expression level of BmrA.

We summarize quantitative accumulation rates and equilibrium times of accumulation of intracellular NPs in single living cells (Figs. 5 and 6) in Table 1, which shows their dependence on the expression level of BmrA, concentrations of NPs, and presence of the inhibitor.

#### Characterization of the viability of single cells

Studies have found that Ag NPs show dose-dependent inhibitory effects on bacterial and tumor cells [35, 49, 50]. Therefore, it is crucial for us to characterize the viability of cells that had been incubated with Ag NPs for hours, ensuring that Ag NPs did not affect the function and viability of the cells, and we indeed studied the membrane transporters (BmrA, BmrA-EGFP) of single living cells.

The viability of cells (WT, BmrA-EGFP,  $\Delta$ BmrA) incubated with NPs throughout the duration of the experiments was characterized using live/dead *bacLight* viability and counting assay. The assay determines the viability of cells by detecting both live and dead cells using SYTO9 nucleic acid stain and propidium iodide, respectively [44]. Observation of the green fluorescence ( $\lambda_{\text{max}}=520$  nm)

of SYTO9 in bacterial cells shows viable cells. In contrast, the display of red fluorescence ( $\lambda_{\text{max}} = 610$  nm) of propidium iodide in bacterial cells indicates dead cells. Representative optical images of the cells (WT-BmrA) incubated in the PBS buffer with 1.4 nM Ag NPs for 4 h (Fig. 7A), show the cells with and without NPs. Their fluorescence images in Fig. 7B illustrate the green

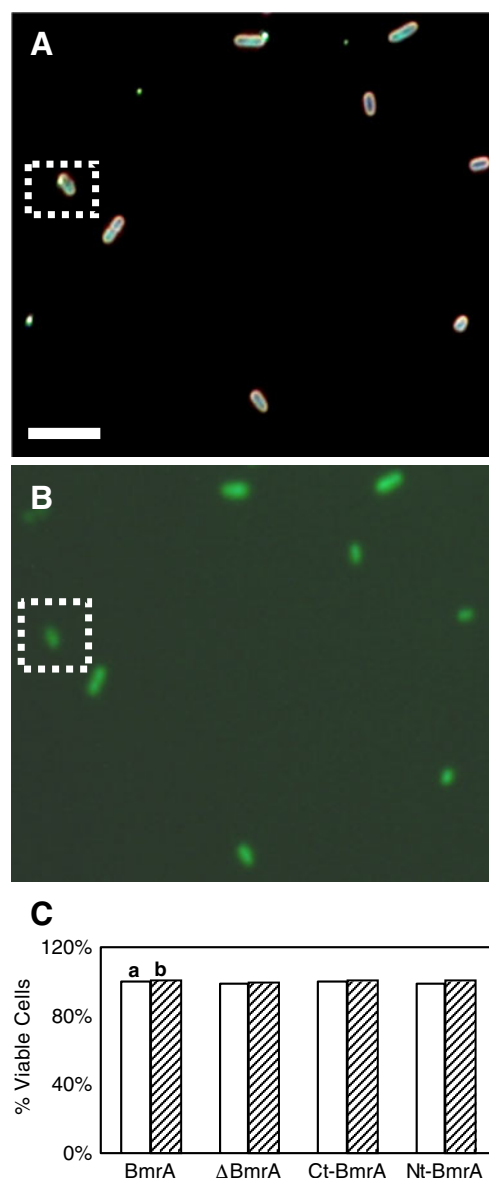


**Fig. 7** Characterization of the viability of single bacterial cells using live/dead *bacLight* viability and counting assay. (A) Dark field optical image and (B) fluorescence image of single bacterial cells (WT-BmrA), incubated with 1.4 nM Ag NPs over the duration of each experiment for 4 h, show that the cells with intracellular NPs (dotted rectangles) or without NPs emit the green fluorescence ( $\lambda_{\text{max}}=520$  nm) of SYTO9, indicating viable cells. (c) Plots of percentage of viable cells at (a) 0 and (b) 4 h, for BmrA,  $\Delta$ BmrA, Ct-BmrA-EGFP, and Nt-BmrA-EGFP cells, show that 99–100% of the cells are alive. A minimum of 900 cells for each strain were assayed at each given time. The scale bars in (A) and (B) are 10  $\mu$ m

fluorescence cells, showing that the cells with and without NPs are alive. Similar phenomena are observed for Ct-BmrA-EGFP, Nt-BmrA-EGFP, and  $\Delta$ BmrA cells.

By counting the number of live and dead cells, we determined the percentage of viable cells by dividing the number of live cells with the total number of the cells. Note that, for each measurement, we assayed at least 900 cells for each strain. The plots of the percentage of viable cells at the beginning and end of experiments in Fig. 7C show that more than 99% of the cells for each strain (WT, Ct-BmrA-EGFP, Nt-BmrA-EGFP, and  $\Delta$ BmrA) were alive and viability remained constant throughout the duration of the experiments, demonstrating that we indeed studied the membrane transporters of single living cells. The results show that the NPs at these selected concentrations (1.4 nM) are biocompatible with the cells, demonstrating that the NPs are well suited for probing of membrane transporters of single living cells in real time.

## Summary

In summary, we have prepared purified and stable (non-aggregation) Ag NPs ( $11.8 \pm 2.6$  nm). In the given doses (1.4 nM), they are biocompatible with the cells. We utilized the size-dependent LSPR spectra of single NPs to determine the sizes of single NPs in and out of single living cells (*B. subtilis*) at nanometer resolution in real time using DFOMS, and to probe size-dependent efflux kinetics of single BmrA membrane transporters (Ct-BmrA-EGFP, Nt-BmrA-EGFP) in single living cells in real-time. The results show that Nt-BmrA-EGFP and Ct-BmrA-EGFP transporters maintain the efflux function of BmrA, offering two new strains for future study of BmrA. We found that the smaller NPs resided longer inside the cells than larger NPs, suggesting the size-dependent efflux kinetics of BmrA and indicating that smaller NPs are more biocompatible with the cells. Furthermore, accumulation and efflux rates of NPs for single living cells are dependent on expression level of BmrA, concentration of NPs, and a pump inhibitor (ortho-vanadate), similar to those observed using a well-known substrate (Hoechst dye) of BmrA transporter, suggesting that NPs are substrates of BmrA transporters and they enter the cells via passive diffusion. Taken together, this study demonstrates that single plasmonic Ag NP optical probes are superior to fluorescent probes for study of efflux kinetics of multidrug membrane transporters in single living cells. Single Ag NPs exhibit size-dependent LSPR spectra and photostability (non-blinking and non-photodecomposition), offering the feasibility of using them to mimic various sizes of antibiotics (drugs) for probing the size-dependent efflux kinetics of membrane transporters of single living cells at nm resolution in real-time for better understanding of MDR.

**Acknowledgements** This work is supported in part by NSF (NIRT: BES 0507036) and NIH (R01 GM076440). Ding, Nallathamby, Browning, and Lee are grateful for the support of Dominion Scholar Fellowship, NIH-GRAS (R01 GM076440S1), and NSF-GRAS (CBET 0940923), respectively. We thank J.-M. Jault for providing us with  $\Delta$ BmrA ( $\Delta$ YvcC) cells, and CharFac of University of Minnesota (a NNIN site funded by NSF) for their assistance in characterizing Ag nanoparticles using HRTEM.

## References

1. Jones PM, George AM (2004) The ABC transporter structure and mechanism: perspectives on recent research. *Cell Mol Life Sci* 61:682–699, and references therein
2. Rees DC, Johnson E, Lewinson O (2009) ABC transporters: the power to change. *Nat Rev Mol Cell Biol* 10:218–227, and references therein
3. Linton KJ, Higgins CF (1998) The *Escherichia coli* ATP-binding cassette (ABC) proteins. *Mol Microbiol* 28:5–13
4. Quentin Y, Fichant G, Denizot F (1999) Inventory, assembly and analysis of *Bacillus subtilis* ABC transport systems. *J Mol Biol* 287:467–484
5. Borst P, Elferink RO (2002) Mammalian ABC transporters in health and disease. *Annu Rev Biochem* 71:537–592
6. Riordan JR, Rommens JM, Kerem B, Alon N, Rozmahel R, Grzelczak Z, Zielenski J, Lok S, Plavsic N, Chou JL et al (1989) Identification of the cystic fibrosis gene: cloning and characterization of complementary DNA. *Science* 245:1066–1073
7. Gottesman MM, Ambudkar SV (2001) Overview: ABC transporters and human disease. *J Bioenerg Biomembr* 33:453–458, and references therein
8. Gottesman MM, Ambudkar SV, Xia D (2009) Structure of a multidrug transporter. *Nat Biotechnol* 27:546–547, and references therein
9. Higgins CF (2001) ABC transporters: physiology, structure and mechanism—an overview. *Res Microbiol* 152:205–210, and references therein
10. Hung LW, Wang IX, Nikaido K, Liu PQ, Ames GF, Kim SH (1998) Crystal structure of the ATP-binding subunit of an ABC transporter. *Nature* 396:703–707
11. Locher KP, Lee AT, Rees DC (2002) The *E. coli* BtuCD structure: a framework for ABC transporter architecture and mechanism. *Science* 296:1091–1098
12. Davidson AL, Chen J (2004) ATP-binding cassette transporters in bacteria. *Annu Rev Biochem* 73:241–268, and references therein
13. Holland IB, Blight MA (1999) ABC-ATPases, adaptable energy generators fuelling transmembrane movement of a variety of molecules in organisms from bacteria to humans. *J Mol Biol* 293:381–399
14. Kunst F, Ogasawara N, Moszer I, Albertini AM, Alloni G, Azevedo V, Bertero MG, Bessieres P, Bolotin A, Borchert S, Borriss R, Boursier L, Brans A, Braun M, Brignell SC, Bron S, Brouillet S, Bruschi CV, Caldwell B, Capuano V, Carter NM, Choi SK, Codani JJ, Connerton IF, Danchin A et al (1997) The complete genome sequence of the gram-positive bacterium *Bacillus subtilis*. *Nature* 390:249–256
15. van Dijk JM, Buist G, Sibbald MJJB, Zweers JC, Dubois JYF, Tjalsma H (2007) Ins and Outs of the *Bacillus subtilis* Membrane Proteome. In: Graumann P (ed) *Bacillus: Cellular and Molecular Biology*. Caister Academic Press, Norfolk, pp 289–332
16. Aguilar C, Vlamakis H, Losick R, Kolter R (2007) Thinking about *Bacillus subtilis* as a multicellular organism. *Curr Opin Microbiol* 10:638–643, and references therein
17. Völker U, Hecker M (2005) From genomics via proteomics to cellular physiology of the Gram-positive model organism *Bacillus subtilis*. *Cell Microbiol* 7:1077–1085



18. Morjani H, Aouali N, Belhoussine R, Veldman RJ, Levade T, Manfait M (2001) Elevation of glucosylceramide in multidrug-resistant cancer cells and accumulation in cytoplasmic droplets. *Int J Cancer* 94:157–165
19. Mortimer PG, Piddock LJ (1991) A comparison of methods used for measuring the accumulation of quinolones by Enterobacteriaceae, *Pseudomonas aeruginosa* and *Staphylococcus aureus*. *J Antimicrob Chemother* 28:639–653, and references therein
20. Orelle C, Gubellini F, Durand A, Marco S, Levy D, Gros P, Di Pietro A, Jault JM (2008) Conformational change induced by ATP binding in the multidrug ATP-binding cassette transporter BmrA. *Biochemistry* 47:2404–2412
21. Steel C, Wan Q, Xu XHN (2004) Single live cell imaging of chromosomes in chloramphenicol-induced filamentous *Pseudomonas aeruginosa*. *Biochemistry* 43:175–82
22. Xu XHN, Brownlow WJ, Huang S, Chen J (2003) Real-time measurements of single membrane pump efficiency of single living *Pseudomonas aeruginosa* cells using fluorescence microscopy and spectroscopy. *Biochem Biophys Res Commun* 305:79–86
23. Cosa G, Focsaneanu KS, McLean JRN, McNamee JP, Scaiano JC (2001) Photophysical properties of fluorescent DNA-dyes bound to single- and double-stranded DNA in aqueous buffered solution. *Photochem Photobiol* 73:585–599
24. Serysheva II, Ludtke SJ, Baker ML, Cong Y, Topf M, Eramian D, Sali A, Hamilton SL, Chiu W (2008) Subnanometer-resolution electron cryomicroscopy-based domain models for the cytoplasmic region of skeletal muscle RyR channel. *Proc Natl Acad Sci USA* 105:9610–9615
25. Huang T, Nallathamby PD, Gillet D, Xu XHN (2007) Design and synthesis of single nanoparticle optical biosensors for imaging and characterization of single receptor molecules on single living cells. *Anal Chem* 79:7708–7718
26. Huang T, Nallathamby PD, Xu XHN (2008) Photostable single-molecule nanoparticle optical biosensors for real-time sensing of single cytokine molecules and their binding reactions. *J Am Chem Soc* 130:17095–17105
27. Kreibitz U, Vollme M (1995) Optical properties of metal clusters. Springer, Berlin
28. Kyriacou SV, Brownlow WJ, Xu XHN (2004) Using nanoparticle optics assay for direct observation of the function of antimicrobial agents in single live bacterial cells. *Biochemistry* 43:140–147
29. Nallathamby PD, Lee KJ, Xu XHN (2008) Design of stable and uniform single nanoparticle photonics for in vivo dynamics imaging of nanoenvironments of zebrafish embryonic fluids. *ACS Nano* 2:1371–1380
30. Xu XHN, Brownlow WJ, Kyriacou SV, Wan Q, Viola JJ (2004) Real-time probing of membrane transport in living microbial cells using single nanoparticle optics and living cell imaging. *Biochemistry* 43:10400–10413
31. Xu XHN, Chen J, Jeffers RB, Kyriacou SV (2002) Direct measurement of sizes and dynamics of single living membrane transporters using nano-optics. *Nano Lett* 2:175–182
32. Browning LM, Lee KJ, Huang T, Nallathamby PD, Lowman J, Xu XHN (2009) Random walk of single gold nanoparticles in zebrafish embryos leading to stochastic toxic effects on embryonic developments. *Nanoscale* 1:138–152
33. Lee KJ, Nallathamby PD, Browning LM, Osgood CJ, Xu XHN (2007) In vivo imaging of transport and biocompatibility of single silver nanoparticles in early development of zebrafish embryos. *ACS Nano* 1:133–143
34. Xu XHN, Song Y, Nallathamby PD (2007) Probing Membrane Transport of Single Live Cells Using Single Molecule Detection and Single Nanoparticle Assay. In: Xu XHN (ed) *New Frontiers in Ultrasensitive Bioanalysis: Advanced Analytical Chemistry Applications in Nanobiotechnology, Single Molecule Detection, and Single Cell Analysis*. Wiley, New Jersey, pp 41–65
35. Nallathamby PD, Xu XHN (2010) Study of cytotoxic and therapeutic effects of stable and purified silver nanoparticles on tumor cells. *Nanoscale* doi:10.1039/c0nr00080a
36. Drew D, Sjostrand D, Nilsson J, Urbig T, Chin CN, de Gier JW, von Heijne G (2002) Rapid topology mapping of *Escherichia coli* inner-membrane proteins by prediction and PhoA/GFP fusion analysis. *Proc Natl Acad Sci USA* 99:2690–2695
37. Gandlur SM, Wei L, Levine J, Russell J, Kaur P (2004) Membrane topology of the DrrB protein of the Doxorubicin transporter of *Streptomyces peucetius*. *J Biol Chem* 279:27799–27806
38. Shukla S, Saini P, Smriti JS, Ambudkar SV, Prasad R (2003) Functional characterization of *Candida albicans* ABC transporter Cdr1p. *Eukaryot Cell* 2:1361–1375
39. Abe-Dohmae S, Ikeda Y, Matsuo M, Hayashi M, Okuhira K, Ueda K, Yokoyama S (2004) Human ABCA7 supports apolipoprotein-mediated release of cellular cholesterol and phospholipid to generate high density lipoprotein. *J Biol Chem* 279: 604–611
40. Steinfels E, Orelle C, Fantino JR, Dalmas O, Rigaud JL, Denizot F, Di Pietro A, Jault JM (2004) Characterization of YvcC (BmrA), a multidrug ABC transporter constitutively expressed in *Bacillus subtilis*. *Biochemistry* 43:7491–7502
41. Xu XHN, Huang S, Brownlow WJ, Salatia K, Jeffers R (2004) Size and temperature dependence of surface plasmon absorption of gold nanoparticles induced by Tris(2, 2'-Bipyridine)Ruthenium (II). *J Phys Chem B* 108:15543–15551
42. Kyriacou SV, Nowak ME, Brownlow WJ, Xu XHN (2002) Single live cell imaging for real-time monitoring of resistance mechanism in *Pseudomonas aeruginosa*. *J Biomed Opt* 7:576–586
43. Xu XHN, Wan Q, Kyriacou SV, Brownlow WJ, Nowak ME (2003) Direct observation of substrate induction of resistance mechanism in *Pseudomonas aeruginosa* using single live cell imaging. *Biochem Biophys Res Commun* 305:941–949
44. Berney M, Hammes F, Bosshard F, Weilenmann HU, Egli T (2007) Assessment and interpretation of bacterial viability by using the live/dead bacLight kit in combination with flow cytometry. *Appl Environ Microbiol* 73:3283–3290
45. Ocaktan A, Yoneyama H, Nakae T (1997) Use of fluorescence probes to monitor function of the subunit proteins of the MexA-MexB-OprM drug extrusion machinery in *Pseudomonas aeruginosa*. *J Biol Chem* 272:21964–21969
46. Steinfels E, Orelle C, Dalmas O, Penin F, Miroux B, Di Pietro A, Jault JM (2002) Highly efficient over-production in *E. coli* of YvcC, a multidrug-like ATP-binding cassette transporter from *Bacillus subtilis*. *Biochim Biophys Acta* 1565:1–5
47. Hochman Y, Carmeli S, Carmeli C (1993) Vanadate, a transition state inhibitor of chloroplast CF<sub>1</sub>-ATPase. *J Biol Chem* 268:12373–12379
48. Urbatsch IL, Tyndall GA, Tomblin G, Senior AE (2003) P-glycoprotein catalytic mechanism: studies of the ADP-vanadate inhibited state. *J Biol Chem* 278:23171–23179
49. Kyriacou SV (2003) Real-time study of multidrug resistance mechanism in *Pseudomonas aeruginosa* using nanoparticle optics and single live cell imaging, Thesis, Department of Chemistry and Biochemistry, Old Dominion University, Norfolk, VA, USA
50. Vaidyanathan R, Kalishwaralal K, Gopalram S, Gurunathan S (2009) Nanosilver—the burgeoning therapeutic molecule and its green synthesis. *Biotechnol Adv* 27:924–937, and references therein